

PROCEEDINGS OF SPIE

[SPIDigitalLibrary.org/conference-proceedings-of-spie](https://spiedigitallibrary.org/conference-proceedings-of-spie)

Algorithm design for image-based wavefront control without wavefront sensing

Orestis Kazasidis, Sven Verpoort, Ulrich Wittrock

Orestis Kazasidis, Sven Verpoort, Ulrich Wittrock, "Algorithm design for image-based wavefront control without wavefront sensing," Proc. SPIE 10695, Optical Instrument Science, Technology, and Applications, 1069502 (28 May 2018); doi: 10.1117/12.2312523

SPIE.

Event: SPIE Optical Systems Design, 2018, Frankfurt, Germany

Algorithm design for image-based wavefront control without wavefront sensing

Orestis Kazasidis^a, Sven Verpoort^a, and Ulrich Wittrock^a

^aPhotonics Laboratory, Münster University of Applied Sciences, Stegerwaldstrasse 39, 48565 Steinfurt, Germany

ABSTRACT

Active optics is an enabling technology for future large space telescopes. Image-based wavefront control uses an image-sharpness metric to evaluate the optical performance. A control algorithm iteratively adapts a corrective element to maximize this metric, without reconstructing the wavefront. We numerically study a sharpness metric in the space of Zernike modes, and reveal that for large aberrations the Zernike modes are not orthogonal with respect to this metric. The findings are experimentally verified by using a unimorph deformable mirror as corrective element. We discuss the implications for the correction process and the design of control algorithms.

Keywords: active optics, adaptive optics, sharpness metrics, aberration compensation, algorithm design

1. INTRODUCTION

The upcoming James Webb Space Telescope (JWST) with a 6.5 m segmented primary mirror will use indirect wavefront sensing via phase diversity for alignment and phasing of the primary mirror segments and of the active secondary mirror. Space telescopes with 10-m-class primary mirrors and high angular resolution are currently discussed for characterization of exoplanets and for Earth observation from the geostationary orbit. Such telescopes will also need to have segmented, lightweight primaries in order to keep mass and stowed volume at bay. Active optics at the primary mirror and/or in a plane conjugate to the primary mirror will be required.

An image-based method could be an alternative or a complement to phase diversity for the active control of a space telescope. Image-based wavefront control without wavefront sensing is typically a blind optimization, where an algorithm iteratively adapts the surface of an active element, in this case an active primary mirror or a deformable mirror in its conjugate plane, to optimize a merit function. The performance of the correction is determined by: 1. the merit function, 2. the control domain, and 3. the algorithm. In this paper we represent the pupil wavefront in Zernike modes and discuss the landscape of our merit function in the space of Zernike modes. In section 2 we define our merit function which is an adaptation of a common sharpness metric. Section 3 describes the simulation process and discusses the merit function for small and large aberrations. In section 4 we compare the simulations with experimental results. Finally in section 5 we discuss the design of our control algorithm.

2. MERIT FUNCTION

Conventional fast adaptive optics measures the wavefront directly, e.g., by using a Shack-Hartmann wavefront sensor. Wavefront information can also be retrieved by using an indirect iterative method (e.g., phase diversity¹). In both cases, the inverse wavefront is applied to the corrective element. Aberration correction without wavefront sensing replaces the requirement for the wavefront by the minimization (or maximization) of a merit function. The merit function evaluates the system performance. Image-based aberration correction without wavefront sensing is typically slower than wavefront-based correction. However, this is not a significant drawback for space active optics operating at a bandwidth much lower than 0.1 Hz that should align the optical telescope, and correct for manufacturing errors and slow drifts caused by thermo-elastic effects. Image-based correction has the advantage that it is free of the non-common path errors of direct wavefront sensing. It neither requires

Further author information: (Send correspondence to Orestis Kazasidis)

Orestis Kazasidis: E-mail: kazasidis@fh-muenster.de, Telephone: +49 2551-962-116

the accurate calibration of an amount of known aberration (commonly defocus) that is a prerequisite of phase diversity. Image-based correction tries to minimize the influence of wavefront aberrations on the image quality and does not try to minimize the aberrations per se. In a situation where the corrective element cannot produce the required wavefront, an image-based method can find a much better solution than methods that measure the aberration and try to compensate it. In this paper, we demonstrate this advantage with an example.

Muller and Buffington² presented several image-sharpness metrics that can serve as merit functions for aberration correction without wavefront sensing. Their S_1 function is the most commonly used image-sharpness metric: $S_1 = \int I(x, y)^2 dx dy$, where $I(x, y)$ is the irradiance at the point (x, y) of the image plane. We discretize this metric for use with a pixelated detector in the image plane. We further normalize it by the square of the total image energy to account for variations of the total photon flux, as discussed by Sulai and Dubra.³ We also multiply by the total number of detector pixels to allow the comparison among images of different number of pixels. Thus we define:

$$MF = - \frac{\sum_{n_x=1}^{N_x} \sum_{n_y=1}^{N_y} I(n_x, n_y)^2}{\left[\sum_{n_x=1}^{N_x} \sum_{n_y=1}^{N_y} I(n_x, n_y) \right]^2} N_x N_y, \quad (1)$$

where x and y are the axes of the image coordinate system, N_x and N_y are the numbers of the pixels in each axis, and I is the pixel value. The minus sign converts the sharpness maximization to a minimization problem.

3. NUMERICAL SIMULATIONS

3.1 Point spread function and image simulation

We simulate the point spread function (PSF) of an imaging system with uniformly illuminated circular aperture in MATLAB⁴ by using the 2-D fast Fourier transform of the pupil function. We choose the width of the diffraction-limited PSF to be 40 pixels, significantly larger than the required width of 5 pixels according to the Nyquist sampling theorem. We limit the total grid to 1201 pixels \times 1201 pixels, i.e., 30 times larger than the diffraction-limited PSF width, in order to reduce the computational cost. We estimate that the error caused by this truncation is negligible. Incoherent images of extended objects can be generated by the 2-D convolution of the extended object and the PSF. The Rayleigh resolution limit equals the diffraction-limited PSF radius, i.e., 20 pixels. In the case of a bar target as object (an example is shown in Fig. 1), the Rayleigh resolution limit corresponds to a linewidth of 10 pixels. The Sparrow resolution limit is about 20% smaller than the Rayleigh limit, i.e., at a linewidth of 8 pixels for a bar target. Figure 1 shows the resolution limits. Here the objects are binary sets of three horizontal and three vertical lines with the specified linewidth. The contrast for the Rayleigh resolution limit is 11% and for the Sparrow resolution limit it is 0%.

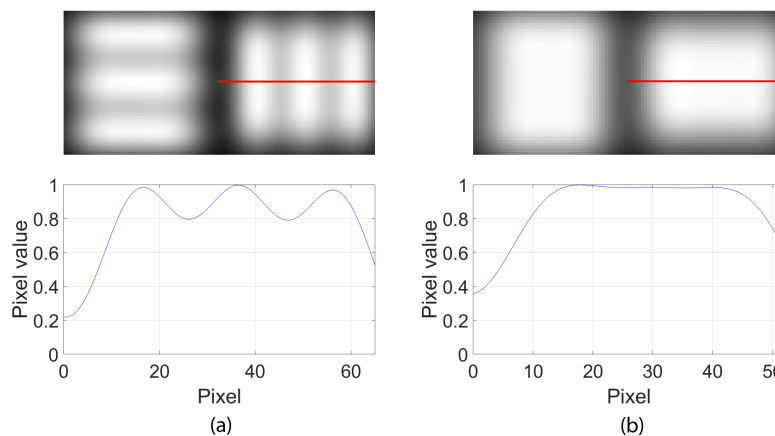


Figure 1. a) The Rayleigh resolution limit with 11% contrast for bars with 10 pixels linewidth. b) The Sparrow resolution limit with 0% contrast for bars with 8 pixels linewidth.

Aberrations in the form of Zernike polynomials are introduced by altering the phase of the complex pupil function. This results in an aberrated PSF that we normalize to the maximum of the diffraction-limited PSF. Throughout this paper, we use the Zernike notation of Wyant and Creath.⁵ Figure 2 shows the pupil wavefronts for 1λ amplitude of the low-order Zernike modes that we will use in this paper. In our Zernike notation, the peak-to-valley (PV) wavefront deformation equals two times the Zernike coefficient value, i.e., $PV_{z_i} = 2 |z_i|$, where in this case $z_i = 1\lambda$. The only exceptions are the Zernike modes with zero radial order and even azimuthal order, e.g., Z_8 - spherical aberration, for which $PV_{z_i, \text{for } (m=0, n \text{ even})} = 1.5 |z_i|$.

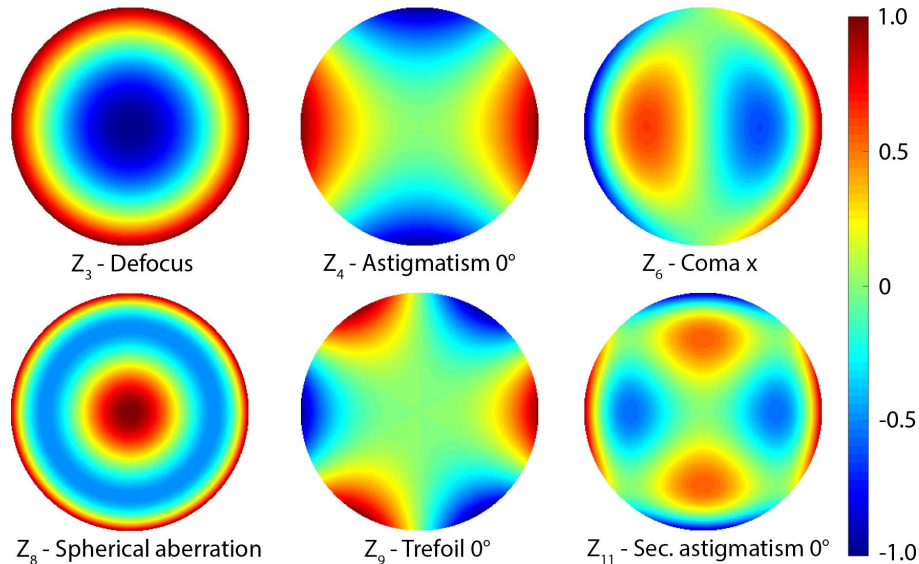


Figure 2. (Color online) The pupil wavefronts for 1λ amplitude of the low-order Zernike modes that we will use in this paper. The common colorbar on the right is in units of λ .

3.2 The merit function in Zernike space

We simulate the incoherent imaging of an extended object as described in the previous paragraph. Our extended object comprises sets of three horizontal and three vertical lines with linewidths of 50 pixels and 20 pixels. The sets of bars with 50 pixels linewidth are rotated by 15° with respect to the object coordinate system. The sets of bars with 20 pixels linewidth are parallel to the object coordinate system and placed near the edges of the object. Thus we span a wide frequency content in the object. Figure 3 shows the diffraction-limited image of our extended object.

We calculate the images in the presence of various combinations of two Zernike mode aberrations in the range $\pm 2\lambda$. The step size for the coefficients of each pair of Zernike modes is 0.1λ , while the coefficients of the rest of the Zernike modes are set to 0. Then we calculate the merit function and observe its 2-D cuts in the Zernike space. Figure 4 shows 2-D cuts of the merit function in the Zernike space for specific pairs of Zernike modes. The global minimum for all cuts is at $(0, 0)$, where we obtain the diffraction-limited image shown in Fig. 3.

Small aberrations

Near the region of the global minimum, the contour lines of the merit function for any pair of Zernike modes are either circles with center at $(0, 0)$ (see Fig. 4a) or ellipses with foci along the Zernike axes and center again at $(0, 0)$ (see Figs. 4b to 4e). This means that the merit function is influenced independently by each Zernike mode, or in other words, that the pairs of Zernike modes are orthogonal to each other with respect to the merit function. Circular contour lines mean that the two Zernike modes have quantitatively the same effect on the merit function, and elliptic contour lines mean that the two Zernike modes have different effect on the merit function. For small aberrations, the Zernike modes are balanced with respect to the Strehl ratio (S), i.e., the effect of each individual Zernike mode on the Strehl ratio is independent of the other Zernike modes.^{6,7} Strehl



Figure 3. The diffraction-limited image of our extended object with sets of three horizontal and three vertical lines with linewidths of 50 pixels and 20 pixels. The contrast is 88 % for the bars with 50 pixels linewidth and 64 % for the bars with 20 pixels linewidth. The image size is 709 pixels \times 461 pixels.

ratio is a measure of the image quality when imaging a point source. Therefore, it is related to our merit function. According to the Maréchal criterion, the range of small aberrations is defined for Strehl ratio greater than 0.8. For Strehl ratio greater than 0.5 the following approximation is valid: $S \approx [1 - 2\pi^2(\sigma/\lambda)^2]^2$, where σ is the standard deviation of the wavefront and λ is the wavelength.⁷

Large aberrations

For large aberrations the approximate formula for the Strehl ratio of the previous paragraph becomes invalid and the Zernike modes are no longer balanced with respect to the Strehl ratio. This is the reason why outside the region of the global minimum our merit function features different landscapes for each pair of Zernike modes, as shown in Fig. 4.

For Z_4 -astigmatism 0° and Z_5 -astigmatism 45° (Fig. 4a) the contour lines of the merit function are circles even for large Zernike coefficients, which means that the two primary astigmatism remain orthogonal to each other with respect to the merit function. This is true for every pair of Zernike modes of the same radial order and opposite azimuthal order, e.g., the two primary comas Z_6 and Z_7 , and the two primary trefoils Z_9 and Z_{10} (not shown).

Far away from the center, the contour lines in Figs. 4b, c, d, and e are neither circles nor ellipses. For these pairs of Zernike modes, the value of one mode that delivers the minimum merit function depends on the value of the other mode. This means that for large Zernike coefficients, these pairs of Zernike modes are not orthogonal to each other with respect to the merit function.

The plot for Z_3 -defocus and Z_4 -astigmatism 0° shown in Fig. 4b has an X-shaped valley for large Zernike coefficients. For a non-zero astigmatism value, there exist two local minima of the merit function, which correspond to two planes where the horizontal lines or the vertical lines of the extended object are in focus. By varying the defocus value we can move from the image with focused horizontal lines ($Z_3 > 0$) via the circle of least confusion ($Z_3 = 0$) to the image with focused vertical lines ($Z_3 < 0$). One example is designated in Fig. 4b: when $Z_4 = 1 \lambda$, the merit function has two local minima for $Z_3 = \pm 0.5 \lambda$. This dependency has already been studied using the variance of the intensity in the image plane as merit function⁸ and we will not go into further detail.

The plot for Z_3 -defocus and Z_8 -spherical aberration shown in Fig. 4c has an almost straight but slightly S-shaped valley for large Zernike coefficients. Again here, the value of Z_3 that delivers the minimum merit function depends on the value of Z_8 . One example is illustrated: when $Z_8 = 0.4 \lambda$, the minimum of the merit

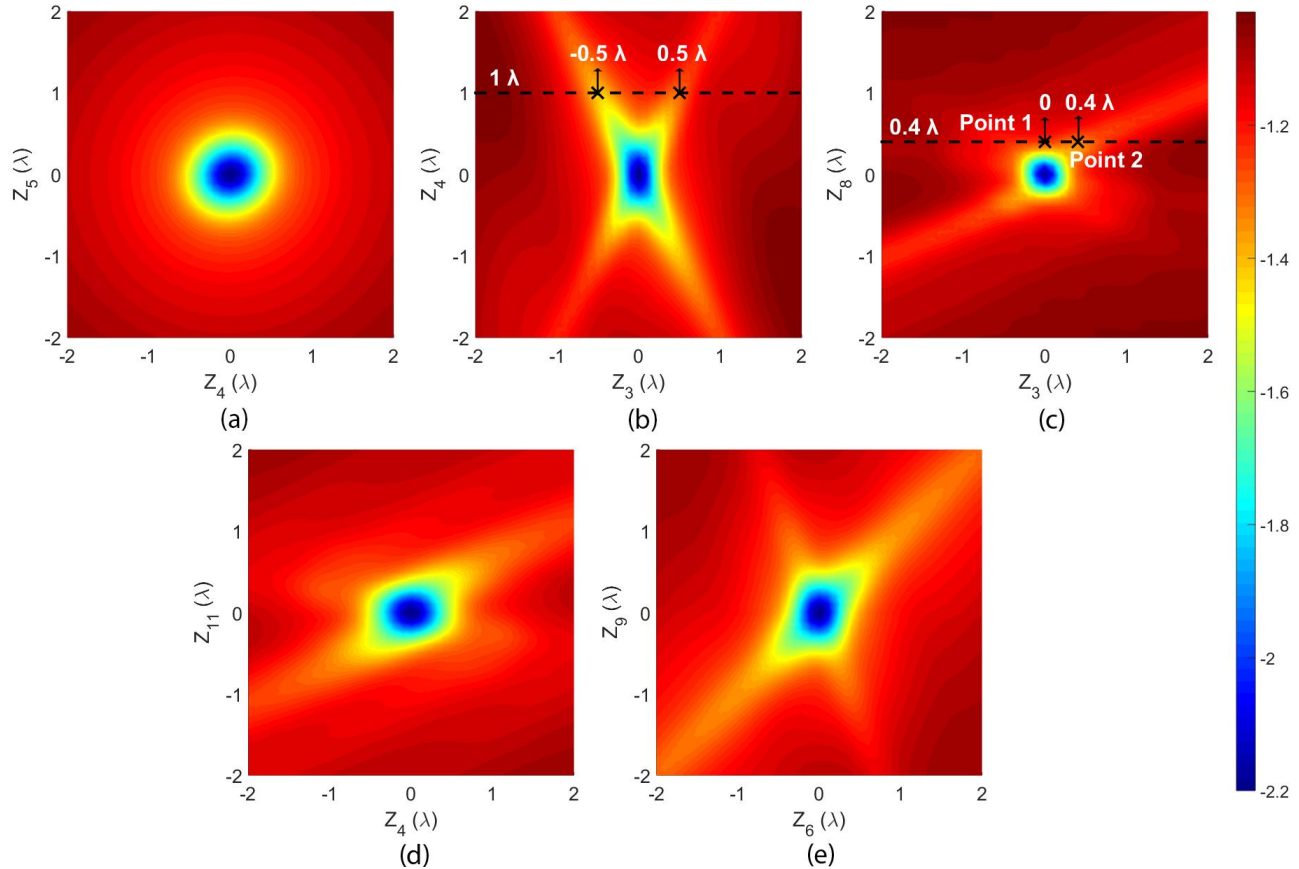


Figure 4. (Color online) 2-D cuts of the merit function in the Zernike space for imaging our extended object. The step size is 0.1λ . Z_3 : defocus, Z_4 : astigmatism 0° , Z_6 : coma x, Z_8 : spherical aberration, Z_9 : trefoil 0° , and Z_{11} : secondary astigmatism 0° .

function is found for $Z_3 = 0.4\lambda$. This means that adding some defocus in the presence of spherical aberration, i.e., going from point 1 to point 2 in Fig. 4c, will deliver a lower (better) merit function and thus a sharper image. In Fig. 5 we examine the aberrated images and the pupil wavefronts delivered at point 1 where $(Z_3, Z_8) = (0, 0.4\lambda)$, and at point 2 where $(Z_3, Z_8) = (0.4\lambda, 0.4\lambda)$. The image corresponding to point 1 of Fig. 4c is shown in Fig. 5a. It has 12% contrast for the bars with 50 pixels linewidth. The bars with 20 pixels linewidth are so blurred that they are not resolved anymore. The image corresponding to point 2 of Fig. 4c is shown in Fig. 5b. It has 40% contrast for the bars with 50 pixels linewidth and 31% contrast for the bars with 20 pixels linewidth. For comparison, the diffraction-limited image for $(Z_3, Z_8) = (0, 0)$ shown in Fig. 3 has a contrast of 88% for the bars with 50 pixels linewidth and 64% for the bars with 20 pixels linewidth. The lower part of Fig. 5 shows the pupil wavefronts corresponding to the aberrated images. The wavefront for $(Z_3, Z_8) = (0, 0.4\lambda)$ shown in Fig. 5c has a PV deformation of 0.6λ and an RMS deformation of 0.18λ . Both PV and RMS deformation of the wavefront for $(Z_3, Z_8) = (0.4\lambda, 0.4\lambda)$ shown in Fig. 5d are larger. The PV deformation is 1.1λ and the RMS deformation is 0.29λ . Despite the larger deviation from the flat wavefront, the pair $(Z_3, Z_8) = (0.4\lambda, 0.4\lambda)$ delivers indeed a sharper image.

In Fig. 4d for the pair Z_4 -astigmatism 0° and Z_{11} -secondary astigmatism 0° we also detect an S-shaped valley for large Zernike coefficients. The two examples in Figs. 4c and 4d reveal that all pairs of Zernike modes of the same azimuthal order are not orthogonal with respect to the merit function. The possibility to use a lower-order Zernike mode to counteract an uncompensated higher-order Zernike mode significantly differentiates image-based aberration correction from aberration correction with wavefront sensing.

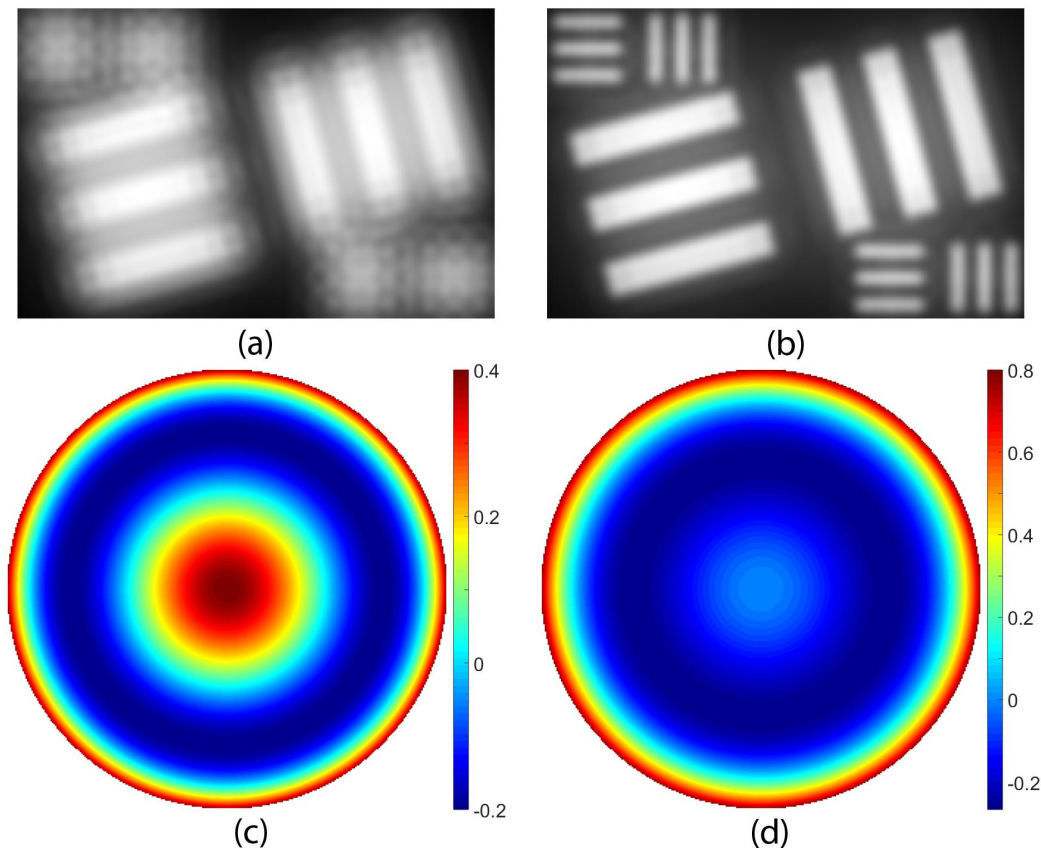


Figure 5. (Color online) Adding defocus in the presence of spherical aberration delivers a sharper image. The aberrated images of our extended object and the pupil wavefronts corresponding to the points 1 and 2 of Fig. 4c. a) Image and c) Wavefront corresponding to point 1 of Fig. 4c, where $(Z_3, Z_8) = (0, 0.4 \lambda)$, $S = 0.12$, and $MF = -1.25$. b) Image and d) Wavefront corresponding to point 2 of Fig. 4c, where $(Z_3, Z_8) = (0.4 \lambda, 0.4 \lambda)$, $S = 0.26$, and $MF = -1.33$. The images are normalized to their maximum value. The colorbars for the wavefronts are in units of λ . Z_3 : defocus and Z_8 : spherical aberration.

The plot for the pair Z_6 -coma x and Z_9 -trefoil 0° (Fig. 4e) has a valley for large Zernike coefficients. The non-orthogonality of Zernike modes of different azimuthal order with respect to the merit function indicates the complexity of the merit function in the Zernike space.

4. EXPERIMENTAL VERIFICATION

We have constructed a testbed to investigate control strategies for image-based aberration correction in a conjugated plane. Figure 6 shows the testbed, whose description will be soon available elsewhere (Kazasidis et al., “Extended-image-based correction of aberrations using a deformable mirror with hysteresis,” manuscript in preparation). The plane of aberration generation (B) is imaged to the plane of aberration correction (B') with a 4-f telescope and a magnification of -1 . The letters A, A' and A'' indicate the image-forming conjugate planes. We use a negative 1951 USAF test target as object. The highest line density of the test target is 228 lp/mm, which should be transmitted by the testbed which has a theoretical cutoff frequency of 290 lp/mm for the wavelength of 633 nm.

In this study the first deformable mirror, called “aberration generator”, is kept open-loop flattened and the second deformable mirror, called “aberration corrector”, is controlled by selecting a 99-Zernike vector and calculating the voltages via the pseudoinverse of the interferometrically measured influence matrix.⁹ There is no simple relation between the optical resolution and the merit function. We find the region of the global minimum

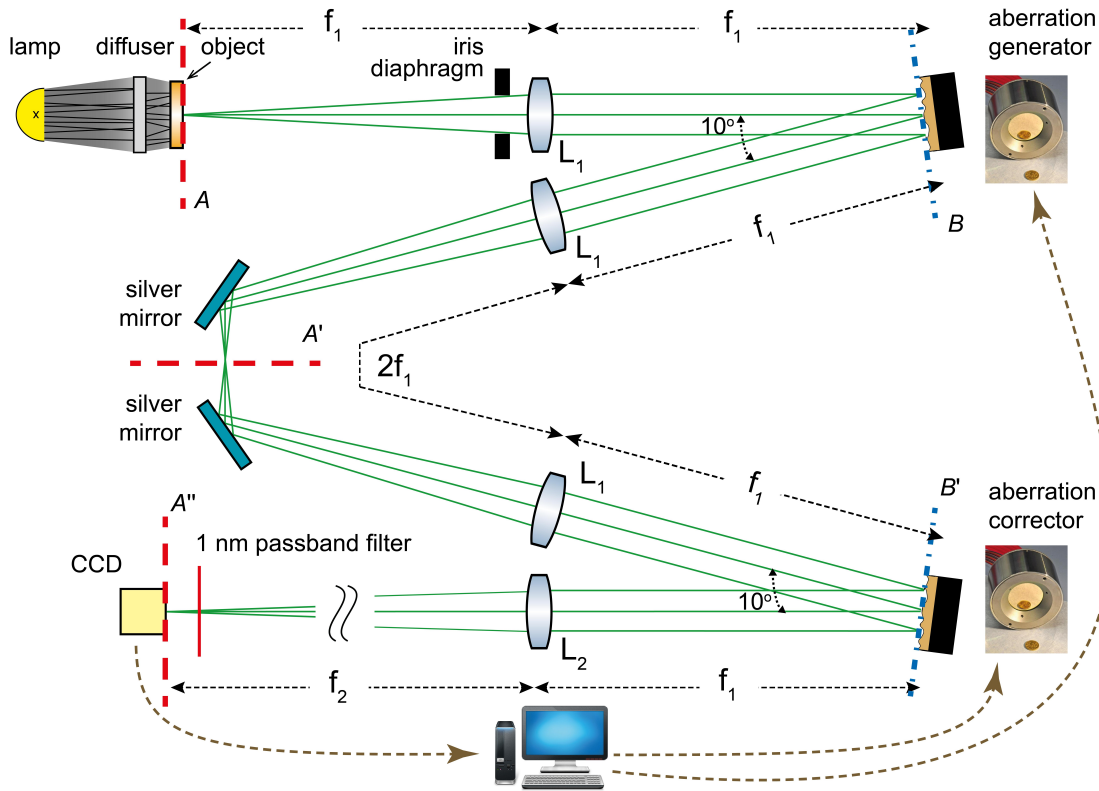


Figure 6. Sketch of the testbed. The plane of aberration generation (B) is imaged to the plane of aberration correction (B') with a 4-f telescope and a magnification of -1 . The letters A, A' and A'' indicate the image-forming conjugate planes. The magnification from plane A to plane A' is -1 , and from plane A' to plane A'' is -3 . The angles of incidence on the deformable mirrors are approximately 5° . The two silver mirrors around plane A' ensure the correct orientation for the conjugation between the planes B and B'. Lens focal lengths: $f_1 = 250$ mm, $f_2 = 750$ mm.

by visually ensuring that the highest line density of the test target is resolved. In Fig. 7b we show the measured merit function for changing Z_3 -defocus in the region of the global minimum for different values of Z_8 -spherical aberration. For $Z_8 = 0$, Z_3 has one minimum at $0 \mu\text{m}$. The merit function is becoming flatter for increasing Z_8 . For $Z_8 > 0.6 \mu\text{m}$, a second minimum appears. We show the plot for $Z_8 = 0.8 \mu\text{m}$ where the second minimum for Z_3 at $1.9 \mu\text{m}$ is smaller than the minimum at 0. For comparison, Fig. 7a shows the results of the simulations, that are 1-D cuts through the Fig. 4c. In both simulation and experiment we see that for a large Z_8 , a non-zero value of Z_3 delivers the minimum (best) merit function. This corresponds to the S-shaped valley of the simulated 2-D cut shown in Fig. 4c. The position and the shape of this valley differ between the simulation and the experiment. We control the deformable mirror open-loop by setting its voltages. The piezoelectric hysteresis is compensated open-loop using the Prandtl-Ishlinskii formalism as described in,¹⁰ thus reduced from 15% to 2%. However, the residual, uncompensated hysteresis limits the system performance. Therefore, the real surface of the mirror can deviate from the desired surface. This reduces the repeatability of the merit function and renders the detection of the valley in the merit function difficult. In addition, in the experiment we image the central part of the negative 1951 USAF test target with the elements of groups 6 and 7 (with line densities from 64 lp/mm to 228 lp/mm). Thus the spatial information of the object differs between the simulation (imaging the object shown in Fig. 3) and the experiment. Further influences for the experimental merit function are the non-normal incidence on the deformable mirror, uncompensated aberrations, system misalignments, and scenes in the object plane just outside the field stop.

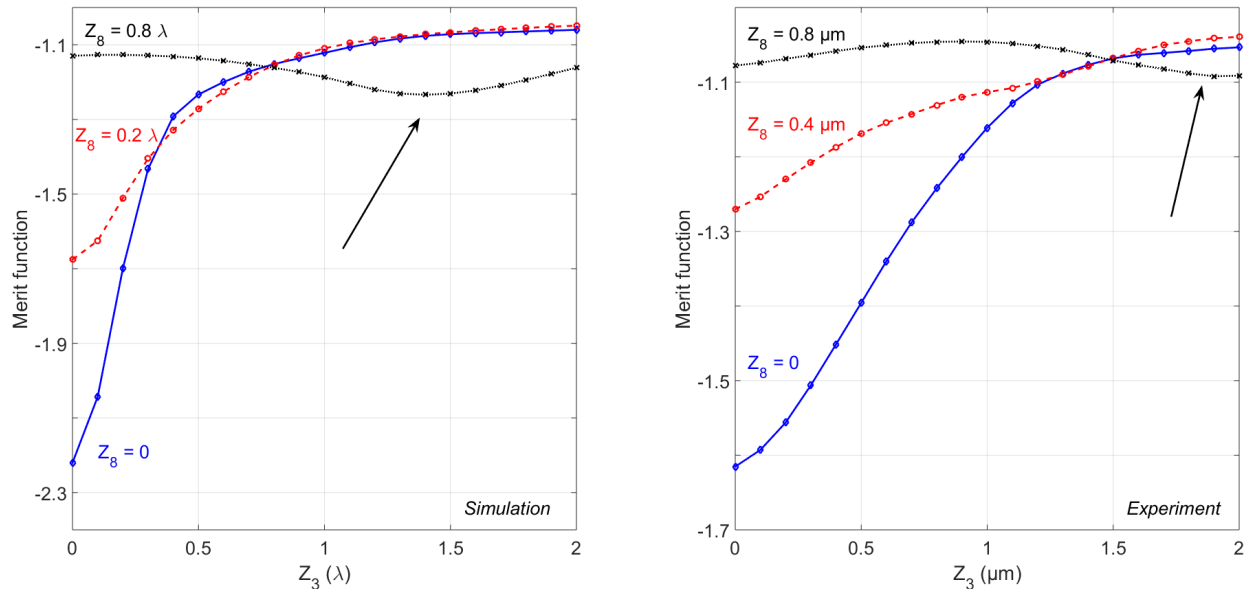


Figure 7. (Color online) The merit function for changing Z_3 -defocus with different values of Z_8 -spherical aberration. Left: Results of numerical simulations, when imaging the artificial extended object whose diffraction-limited image is shown in Fig. 3. The plots are 1-cuts through the Fig. 4c. The step size is 0.1λ . Right: Experimental results, when imaging the central part of the negative 1951 USAF test target with the testbed shown in Fig. 6. The step size is $0.1 \mu\text{m} \approx 0.16 \lambda$. The arrows in both plots indicate a valley outside the region of the global minimum.

5. ALGORITHM DESIGN

The cuts of the merit function in the multi-dimensional Zernike space are crucial for the algorithm design, revealing valleys that may slow down or trap the algorithm. The global minimum is for zero aberration. A population-based global search algorithm, such as an evolutionary algorithm, can in principle solve the problem fast and efficient. However, the hysteresis left over after the open-loop compensation discussed in Section 4 leads to low repeatability of the merit function, especially in the steep region of the global minimum. Therefore the performance of these population-based algorithms in our system is limited. On the other hand, trajectory-based global search algorithms that need large jumps, such as simulated annealing, experience problems if the actuators have hysteresis. Therefore, we are currently using the simple heuristic hill descending technique in separate Zernike modes, as presented in routine 1. Our algorithm calculates the two-sided univariate differentials of the merit function. It then runs a hill descending optimization in the direction of the minimum negative differential, i.e., the steepest descent. When this optimization has converged, this Zernike mode is removed from the search space and the routine iterates through the rest of the Zernike modes. The routine ends when all the Zernike modes have been optimized, or when all the two-sided univariate differentials are positive, i.e., the merit function at the current point is smaller than that at every candidate point. The routine is repeated until no further improvement is found.

Our algorithm optimizes the Zernike modes separately in order to reduce the complexity. We select the Zernike mode to be optimized after calculating all the two-sided univariate differentials in order to avoid valleys caused by the non-orthogonality of the Zernike modes with respect to the merit function. Therefore, for example in the case of pure spherical aberration, the algorithm will detect an improvement for changing the defocus, but will prefer changing first the spherical aberration that leads to a larger improvement of the merit function. In the case of large aberrations, the algorithm descends slowly with a zig-zag movement along valleys that are formed for a pair of Zernike modes, e.g., the X-shaped valley for Z_3 and Z_4 shown in Fig. 4b. The algorithm may also be trapped in plateaus if the valley is flattened, or if the step size is not small enough. We can prevent this by first using a global search algorithm to find the valley of the global minimum and then using our steepest descent in separate Zernike modes to detect its exact position.

Routine 1 The steepest descent in separate Zernike modes. N is the number of Zernike modes, \vec{z}_i is the initial point, and \vec{s} is the step size.

```

1: procedure STEEPEST DESCENT IN SEPARATE ZERNIKE MODES( $N, \vec{z}_i, \vec{s}$ )
2:   define set  $E = \{1, \dots, N\}$ 
3:    $\vec{z}_o = \vec{z}_c = \vec{z}_i$  ▷ optimum, current, and initial point in the Zernike space
4:   calculate  $MF(\vec{z}_o)$ 
5:   while  $E \neq \emptyset$  do ▷ Terminate when E is empty
6:     for  $k \in E$  do ▷ Find candidate points
7:        $\vec{z}_{k+} = (z_{o,1}, \dots, z_{o,k} + s_k, \dots, z_{o,N})$ 
8:        $\vec{z}_{k-} = (z_{o,1}, \dots, z_{o,k} - s_k, \dots, z_{o,N})$ 
9:        $MF(\vec{z}_{k=p}) = \min_k \{MF(\vec{z}_{k+}), MF(\vec{z}_{k-})\}$  and  $\vec{z}_c = \vec{z}_{k=p}$  ▷  $p$  is the Zernike mode for which the
        minimum MF among all candidate points is found
10:      if  $MF(\vec{z}_c) < MF(\vec{z}_o)$  then
11:        descend hill in Zernike mode  $p$  in direction of steepest descent, till no further improvement of  $MF$ 
12:         $E = E - p$  and  $\vec{z}_o = \vec{z}_c$  ▷ Reduce set of Zernike modes and replace optimum point
13:      else
14:        break
15:  return  $\vec{x}_o, MF(\vec{x}_o)$ 

```

6. CONCLUSIONS

The selection of the merit function for image-based aberration correction without wavefront sensing should be application-driven. Our results indicate that its landscape should be carefully studied not only near the global minimum for zero aberration, but also for large aberrations. Several merit functions have been proposed for image-based aberration correction, such as the image variance,⁸ the Fourier distribution, and the generalized sharpness metrics proposed by Fienup and Miller¹¹ that exploit the expected characteristics of the object. Here, we used a common image-sharpness metric as merit function. In the presence of large aberrations the Zernike modes are not orthogonal to each other with respect to our merit function. This leads to valleys in the merit function landscape that may slow down or trap the control algorithm. On the other hand, the non-orthogonality with respect to the merit function can be advantageous for image-based correction without wavefront sensing. We demonstrated that, in contrast to aberration correction with wavefront sensing, image-based aberration correction improves the image quality by adding a lower-order Zernike mode to counteract an uncompensated higher-order Zernike mode of the same azimuthal order. This image improvement can be beneficial for optical systems with large aberrations that operate with low Strehl ratio.

This study primarily aims at science imaging with space telescopes using active optics. However, its results are also relevant for Earth observation, wavefront-sensorless adaptive optics in microscopy, optical coherence tomography, and ophthalmoscopy that use a sharpness metric as merit function. Due to the non-orthogonality of the Zernike modes with respect to the merit function for large Zernike coefficients a single iteration of the Zernike modes is not sufficient.

ACKNOWLEDGMENTS

The authors thank Michel Verhaegen, Gleb Vdovin, Oleg Soloviev, Peter Rausch, and Christian Vorholt for discussion and support. This work is supported by the funding programme “Qualifizierungsstelle” of Münster University of Applied Sciences.

REFERENCES

- [1] Dean, B. H. and Bowers, C. W., “Diversity selection for phase-diverse phase retrieval,” *J. Opt. Soc. Am. A* **20**(8), 1490–1504 (2003).
- [2] Muller, R. A. and Buffington, A., “Real-time correction of atmospherically degraded telescope images through image sharpening,” *J. Opt. Soc. Am.* **64**(9), 1200–1210 (1974).

- [3] Sulai, Y. N. and Dubra, A., “Non-common path aberration correction in an adaptive optics scanning ophthalmoscope,” *Biomed. Opt. Express* **5**(9), 3059–3073 (2014).
- [4] MATLAB, [*version 8.5.0 (R2015a)*], The MathWorks Inc., Natick, Massachusetts (2015).
- [5] Wyant, J. C. and Creath, K., “Basic wavefront aberration theory for optical metrology,” in [*Applied Optics and Optical Engineering*], Shannon, R. R. and Wyant, J. C., eds., **11**, ch. 1, Academic Press, Inc., New York (1992).
- [6] Born, M. and Wolf, E., [*Principles of Optics*], 522–527, Cambridge University Press, 7 ed. (2005).
- [7] Williams, C. S. and Becklund, O. A., [*Introduction to the Optical Transfer Function*], 219–237, SPIE Press, Bellingham, Wash., repr. from the 1989 original publ. ed. (2002).
- [8] Erasmus, S. J. and Smith, K. C. A., “An automatic focusing and astigmatism correction system for the SEM and CTEM,” *Journal of Microscopy* **127**, 185–199 (1982).
- [9] Rausch, P., Verpoort, S., and Wittrock, U., “Unimorph deformable mirror for space telescopes: design and manufacturing,” *Opt. Express* **23**(15), 19469–19477 (2015).
- [10] Krejci, P. and Kuhnen, K., “Inverse control of systems with hysteresis and creep,” *IEE Proceedings - Control Theory and Applications* **148**(3), 185–192 (2001).
- [11] Fienup, J. R. and Miller, J. J., “Aberration correction by maximizing generalized sharpness metrics,” *J. Opt. Soc. Am. A* **20**(4), 609–620 (2003).